PCCP

Accepted Manuscript

ROYAL SOCIETY OF CHEMISTRY

www.rsc.org/pccp

Timescales of N-H bond dissociation in pyrrole: a nonadiabatic dynamics study

Marin Sapunar,[a] Aurora Ponzi, [b] Sermsiri Chaiwongwattana,[a] Momir Mališ,[a] Antonio Prlj,[c] Piero Decleva,[b] and Nađa Došlić,*[a]

Received Xth XXXXXXXXXX 20XX, Accepted Xth XXXXXXXXX 20XX
First published on the web Xth XXXXXXXXXX 200X
DOI: 10.1039/b000000x

The excitation wavelength dependent photodynamics of pyrrole are investigated by nonadiabatic trajectory-surface-hopping dynamics simulations based on time dependent density functional theory (TDDFT) and the algebraic diagrammatic construction method to the second order (ADC(2)). The ADC(2) results confirm that the N-H bond dissociation occurring upon excitation at the origin of the first excited state, $S_1(\pi\sigma^*)$, is driven by tunnelling [Roberts *et al.* Faraday Discuss. 2013, **163**, 95] as a barrier of $\Delta E = 1780$ cm^{-1} traps the population in a quasi-bound minimum. Upon excitation to $S_1(\pi\sigma^*)$ in the wavelength range of $236-240$ nm, direct dissociation of the N-H bond takes place with a time constant of 28 fs. The computed time constant is in very good agreement with recently reported measurements. Excitation to the lowest B_2 state in the $198-202$ nm range returns a time constant for N-H fission of 48 fs at the B3LYP/def2-TZVPD level, in perfect agreement with the experiment [Roberts *et al.* Faraday Discuss. 2013, **163**, 95]. For the same wavelength range the ADC(2)/aug-cc-pVDZ decay constant is more than three times longer than the experimentally reported one. The accuracy of the B3LYP/def2-TZVPD dynamics is checked against reference complete-active-space second-order perturbation theory (CASPT2) calculations and explained in terms of correct topography of the $\pi\pi^*$ surface and the lack of mixing between the $\pi\pi^*$ and the $3p_x$ Rydberg states which occurs in the ADC(2) method.

1 Introduction

Pyrrole is a simple five-membered heterocycle found as a structural subunit of larger chromophores. The circular arrangement of four pyrrole units bridged by methine linkers forms the porphyrin macrocycle, the central unit of the heme, cytochrome c, and chlorophyll a chromophores, while bilin, the chromophore of phytochromes, is composed of a quasi-linear arrangement of four pyrroles.[1] The presence of pyrrole in these compounds has prompted many experimental[2–9] and theoretical[10–16] investigations, for it is of major interest to consider whether the photoinduced dynamics of pyrrole can be related to those of complex pyrrole-containing chromophores.

The photochemistry of pyrrole is a textbook example of $^1\pi\sigma^*$ mediated internal conversion.[17–20] In the $A_2(\pi\sigma^*)$ state, which is the first excited state (S_1) of pyrrole,[21–23] the electronic excitation is localized along the N-H bond. After excitation to this state, stretching of the N-H bond leads to a conical intersection (CI) seam between S_1 and the ground electronic state (S_0).

The time scale of H-elimination from the S_1 state was first determined by Lippert *et al.*[4] Two time constants ($\tau_1 = 110 \pm 80$ fs and $\tau_2 = 1.1 \pm 0.5$ ps) for NH fission after excitation at $\lambda = 250$ nm were reported. The first was assigned to direct H-atom detachment along the $S_1(\pi\sigma^*)$ surface, while the second was attributed to H-atom elimination from vibrationally excited molecules in the ground electronic state. More recent experiments provided evidence for only one deactivation time constant.[7,9] Roberts *et al.* used time-resolved ion yield and velocity map imaging techniques to retrieve information on the energetics and time scales of H-elimination at multiple excitation wavelengths. The excitation wavelength dependent time constants for N-H bond fission have been obtained from the kinetic fit of the normalized H$^+$ signal transient (REMPI probed H-atoms) as a function of pump-probe delay time. The exponential rise of the H$^+$ signal at positive pump-probe delay times revealed single time constants of $\tau = 126 \pm 28$ fs and $\tau = 46 \pm 22$ fs for H-elimination at 250 nm (band origin) and 238 nm, respectively.[7] The authors also investigated the dynamics of monodeuterated pyrrole (pyrrole-d_1) and reported a time constant of 1.4 ± 0.3 ps for N-D dissociation at 250 nm giving rise to a kinetic isotope effect of $KIE \approx 11$. These results are consistent with the existence of a small exit barrier on the S_1 surface. Very recently, Wu *et al.*[9] studied the photoin-

---

[a] *Department of Physical Chemistry, Ruđer Bošković Institute, HR-10000 Zagreb, Croatia. Fax: 385 1468 0245; Tel: 385 1456 1038; E-mail: nadja.doslic@irb.hr*
[b] *Dipartimento di Scienze Chimiche, Università di Trieste, I-34127 Trieste, Italy.*
[c] *Ecole polytechnique fédérale de Lausanne, CH-1015 Lausanne, Switzerland.*

duced dynamics of pyrrole using time-resolved photoelectron spectroscopy (TRPES). Following excitation at 242 and 236 nm TRPES spectra disclosed single time constants of 12 and 19 fs, respectively.

In contrast, two time constants of $\tau_1 = 52 \pm 12$ fs and $\tau_2 = 1.0 \pm 0.4$ ns have been reported following excitation of the bright $B_2(\pi\pi^*)$ state at $\lambda = 200$ nm.[7] The first was assigned to fast internal conversion *via* sequential $\pi\pi^* \rightarrow \pi\sigma^* \rightarrow N-H$ processes, while the second was assigned to H-elimination from vibrationally excited ground state species.

The mechanisms and time scales of H-atom elimination from pyrrole have been the subject of both quantum mechanical[9–11,15] and mixed quantum-classical studies.[12–14] Starting from the first excited $A_2(\pi\sigma^*)$ state, Frank and Damianos performed molecular dynamics simulations based on restricted open-shell Kohn-Sham (ROKS) theory.[12] Apart from fast ejected H-atoms ($\approx$ 100 fs) ROKS simulations have shown that a barrier on the S_1 surface leads to trapping of population in the local minimum near the Franck-Condon region which the authors proposed as a source of slow H-atoms. The multiconfigurational Ehrenfest dynamics simulation of Saita *et al.*[16], using the complete active space SCF method (CASSCF), showed dissociation from S_1 with half of the population transferring to the ground state within ≈ 40 fs. Very recently, a similar time constant of 35 fs has been computed using the multiconfiguration time-dependent Hartree (MCTDH) method on a model Hamiltonian constructed using CASPT2 and equation-of-motion (EOM) coupled cluster single- and double-excitation (CCSD) data points.[9] The authors also considered the decay upon excitation at 217 nm. Here two time constants of τ_1= 13 fs and $\tau_2 = 29$ fs were reported for a sequential decay from the $B_1(\pi\sigma^*)$ to the $A_2(\pi\sigma^*)$ state and subsequent decay to the ground state.

The dynamics following excitation of the $B_2(\pi\pi^*)$ needs to account for nonadiabatic transitions among excited electronic states. Simulations have been performed by using the surface-hopping approach coupled to multireference (MR) configuration interaction (CI) and TDDFT methods for electronic structure determination.[13,14] The MRCI-based simulations of Vazdar *et al.*[13] were initiated mostly (60%) in the bright $B_2(\pi\pi^*)$ state and revealed three deactivation mechanisms: N-H bond fission, which was found to be the dominant mechanism, ring puckering and planar ring-opening, leading to 140 fs deactivation to the ground state. The TDDFT-based dynamics of Barbatti *et al.*[14] again revealed a rather slow H-elimination taking place in $\tau \approx 180$ fs in agreement with previous MRCI-based calculations. A somewhat faster deactivation ($\tau \approx 100$ fs) of the $B_2(\pi\pi^*)$ was obtained by Faraji *et al.*[15] The authors employed the MCTDH method and the underlying potential energy surfaces were computed using MRCI.

Given the prototype character of pyrrole, the discrepancy between the computed and measured time constants is disappointing and needs to be better understood. With this aim we re-investigated the photodynamics of pyrrole taking place upon excitation in the wavelength range of $250-196$ nm. In particular, we focus on the nature of the electronic excitation in the $B_2(\pi\pi^*)$ state which is expected to have a direct effect on the dynamics. For well separated valence and Rydberg states, as predicted by multi state (MS) CASPT2 computations, the deplanarization of the five-membered ring will lead to stabilization of the valence $B_2(\pi\pi^*)$ state and destabilization of the Rydberg states.[22,24] On the contrary, planar geometries will be favored in case of strong Rydberg-valence interaction, as obtained with CC methods. Since full-dimensional dynamics simulations based on CASPT2 and EOM-CCSD calculations are unaffordable for pyrrole, we address the problem by employing two effective electronic structure methods with different extents of Rydberg-valence mixing. On the one hand, we used TDDFT and took advantage of the strong sensitivity of Rydberg states on the choice of the basis set to simulate the dynamics on a potential energy surface with weak Rydberg-valence interaction.[25] On the other hand, we investigated the dynamics by using the algebraic diagrammatic construction method to the second order (ADC(2))[26,27] which gives results comparable to the CC2 method and yields strong Rydberg-valence interaction. By comparing the time constants for internal conversion obtained with the two methods with the experimental ones, we are able to provide an insight into the nature of pyrrole's excited electronic states from the dynamics perspective and considerably reduce the gap between theory and experiments.

2 Computational Methods

2.1 Electronic Structure Methods

The ground state equilibrium geometry of pyrrole and the corresponding Hessian matrix were computed using the second-order Møller-Plesset (MP2) method and the augmented correlation consistent polarized valence triple zeta basis set (aug-cc-pVTZ) as implemented in the Turbomole 6.4[28] package. Excited state computations were performed employing two electronic structure methods: the ADC(2) method[26,27] with the resolution of identity approximation (RI)[29–31] and TDDFT with the B3LYP functional[32].

The applicability of both methods for excited state calculations is well documented.[33,34] In the specific case of pyrrole, both methods are suitable for describing the low lying valence and Rydberg states as these states are dominated by single excitations[23,25] and the approximation that the reference ground state should be a single-determinant state is valid for a wide range of geometries that the system explores during the dynamics. The single-determinant description of the ground state is clearly not valid at the conical intersection between the ground and first excited state. Thus, dynamics calculations were stopped when the energy gap between the S_1 and S_0 states dropped below 0.1 eV and this time was taken as the time of internal conversion. Note, however, that conical intersections between excited states are correctly described by both methods as long as the ground state is well described by a single-determinant. To estimate the multireference character of the ground state, D1 diagnostics were calculated.[28,35] Also, we used the λ diagnostic of Peach and Tozer to test TD-B3LYP calculations and trace geometries and electronic states for which errors in the excitation energies are more likely to occur.[36–38]

The challenge to theory is the description of the mixing between the $3p$ Rydberg and the $B_2(\pi\pi^*)$ states. Within TD-B3LYP the description of the Rydberg states and the extent of Rydberg-valence interaction is basis set dependent. Therefore, a range of basis sets has been used to compute the vertical excitation energies (Table S1 and S2) and the results were tested against reported CASPT2 and EOM-CCSD data.[22,23,39] Five method/basis set choices were found suitable for subsequent nonadiabatic (NA) simulations as well as illustrative of the underlying dynamics. The ADC(2) simulations have been performed using aug-cc-pVDZ and cc-pVTZ with diffuse functions of p, d, and f type added to the center of mass of the molecule[40,41] (denoted cc-pVTZ+, the exponents and contraction coefficients are given in Table S3). TDDFT-based calculations have been carried out by employing three basis sets that give rise to different Rydberg-valence interactions: the Turbomole triple-zeta valence basis set with polarized and diffuse functions (def2-TZVPD), the quadruple-zeta basis set with no diffuse functions (def2-QZVP(-f-g)), and the aug-cc-pVTZ basis set.[42,43] To facilitate the computation, the f and g basis functions were not included in the def2-QZVP(-f-g) basis set as it was found that they have little influence on the vertical excitation energies and oscillator strengths.

Further, the accuracy of the potential energy surfaces underlying dynamics simulations has been assessed by comparing the excitation energies for sets of geometries along representative nonadiabatic trajectories with the reference CASPT2/aug-cc-pVDZ data. CASPT2 excited states were calculated using the Molpro package.[44] The CASSCF reference orbitals were obtained in the state-averaged mode (SA-MCSCF). The active space consisted of 8 electrons in 8 orbitals and only the 1s core molecular orbitals were frozen. In the CASPT2 calculations, each state was treated separately and a level shift of 0.3 E_h was applied to the residuals. In all calculations the aug-cc-pVDZ basis set was used.[43]

2.2 Nonadiabatic Dynamics

NA dynamics is a mixed quantum-classical approach in which the electrons are treated quantum mechanically and the nuclei classically. We performed NA dynamics simulations with Tully's fewest switching surface hopping procedure[45] using an in-house code interfaced to Turbomole 6.4.[28] To interface the ADC(2) method with NA dynamics we followed Plasser, Barbatti and co-workers[46] and constructed a formal CIS wave function using ADC(2) singles amplitudes stored in the Turbomole output files. The computation of the NA couplings, thus, reduces to evaluation of overlaps between singly excited Slater determinants. Note that a formal CIS wave function construct is also used to compute the NA couplings at the TDDFT level.[47–49]

For the nuclear motion, Newton's equations were integrated in time steps of $\tau_1 = 0.5$ fs by using the velocity-Verlet algorithm. The energies and the gradients, needed for the propagation of the classical trajectories were computed with the time step of nuclear motion. The elements of the nonadiabatic coupling matrix were calculated from wave function overlaps at two time steps of the nuclear dynamics as described in previous studies.[50–53] The time evolution of the expansion coefficients of the electronic states was computed by integrating the time-dependent Schrödinger equation using Shampine and Gordon's predictor-corrector ordinary differential equation solver algorithm[54] in steps of $\tau_2 = 5 \times 10^{-5}$ fs. Due to enhanced numerical stability, the hopping probabilities were computed at each time step of electronic motion τ_2 as proposed by Mitrić *et al.*[55]

The selection of initial conditions is an important issue in NA dynamics simulations. Here, a set of 2000 initial conditions was generated starting from the ground state Wigner function $f_w(p,q) = \rho_w(p,q)/(2\pi\hbar)$, where

$$\rho_w(p,q) = 2\tanh(\hbar\omega/2kT)e^{-\tanh(\hbar\omega/2kT)(\frac{m\omega}{\hbar}q^2+\frac{1}{m\omega\hbar}p^2)} \quad (1)$$

is the Wigner distribution for the harmonic oscillator thermal density and m and ω are the oscillator mass and frequency.[56] All simulations have been performed at $T = 293$ K. The Hessian matrix was computed at the MP2/aug-cc-pVTZ level. The computed vibrational levels and accompanying Boltzmann population factors are given in Table S4. The $3N-6$ normal modes were sampled independently in accord to Eq.(1) and the normal mode coordinates and velocities were transformed to their Cartesian counterparts.[57,58] On the basis of these geometries, the electronic absorption spectra encompassing the lowest 10 excited states (see Table 1) were calculated using the selected method/basis set combination according to the semiclassical approach proposed by Barbatti *et al.*[59] To simulate the excitation wavelength dependence of the relaxation dynamics we considered three spectral windows centered (±2 nm) at $\lambda = 250$, 238 and 200 nm. Initial conditions for the dynamics were selected from the generated set of ground state geometries by a weighted random algorithm according to the oscillator strengths of the transitions that fit the selected windows. In other words, if several closely spaced electronic states fall into the same energy window the algorithm will preferentially populate the state with the larger oscillator strength. In the low-energy region all trajectories were started from the $S_1(\pi\sigma^*)$ state and propagated in the subspace of the ground and three excited electronic states for a total simulation time of 500 fs. In the $\lambda = 200 \pm 2$ nm window, 100 initial conditions were selected almost exclusively from the bright B_2 state due to its large oscillator strength. In this window ADC(2) (B3LYP) trajectories were propagated in the manifold of the ground and 9 (7) excited electronic states. The same selection criteria and number of trajectories were used for each of the method/basis set choices.

3 Results and Discussion

3.1 Electronic structure calculations

A comparison of the lowest 10 ADC(2)/aug-cc-pVDZ and B3LYP/def2-TZVPD vertical excitation energies with previously reported values is shown in Table 1. The vertical excitation energy of the $S_1(\pi\sigma^*)$ state of 5.13 eV (242 nm) and 4.99 (249 nm) at the ADC(2)/aug-cc-pVDZ and B3LYP/def2-TZVPD levels, respectively, find very good agreement with benchmark theoretical values[22,23,39] and experimental data.[60,61] The ADC(2)/aug-cc-pVDZ minimum of the $S_1(\pi\sigma^*)$ state is located at 4.82 eV (257 nm) and characterized by an N-H bond distance of 1.058 Å. On the other hand, B3LYP fails to locate a minimum on the $S_1(\pi\sigma^*)$ surface.

The ordering of higher excited states in pyrrole is, to some extent, controversial. Using MS-CASPT2, Roos *et al.* found that the $B_2(\pi\pi^*)$ state below the first Rydberg series.[22] On the contrary, general-model-space (GMS) and EOM-CCSD studies predict the $B_2(\pi\pi^*)$ state above the lowest Rydberg states.[23] Recently, Neville and Worth calculated the absorption spectrum of pyrrole using wave packet propagation on model potential energy surfaces constructed using CASPT2/aug-cc-pVDZ+ and EOM-CCSD/aug-cc-pVDZ data points.[39] A good agreement with the experimental spectrum was found showing that the vertical excitation energy of the $B_2(\pi\pi^*)$ state can be as high as 6.24 eV. Our ADC(2)/aug-cc-pVDZ and B3LYP/def2-TZVPD vertical excitations of 6.35 and 6.32 eV, respectively, find good agreement with Neville and Worth.[39]

Despite vertical energies being similar, the nature of the excited states is significantly different. At the B3LYP/def2-TZVPD level all states have a well defined character. At the ADC(2)/aug-cc-pVDZ level, however, considerable mixing between the valence and the Rydberg states was found, with the bright B_2 state having mostly a Rydberg $3p_x$ character. This difference is due to the employment of the def2-TZVPD basis set and not the B3LYP functional that was used in the calculations. The augmented def2 series of basis sets contains diffuse s and d functions, but lacks diffuse p functions. The aug-cc-pVNZ (N = D,T,Q) basis sets do contain diffuse p functions which enhance mixing of $B_2(\pi\pi^*)$ and Rydberg $B_2(\pi 3p_x)$ states. Let us note that, when the ADC(2) method is used with the def2 basis sets the mixing is removed, but the vertical excitation energies are severely overestimated. On the other hand, B3LYP used with the aug-cc-pVTZ basis sets yields mixed states and underestimated vertical excitation energies (see Table S1 and S2).

The minimum energy geometry of the $B_2(\pi\pi^*)$ state strongly depends on the character of the state. B3LYP/def2-TZVPD yields a non-planar minimum 0.7 eV below the vertical excitation energy in agreement with the results of Celani and Werner.[24] When the state has a more significant Rydberg character, such as in ADC(2)/aug-cc-pVDZ, the minimum is planar and found only 0.34 eV below the energy of vertical excitation. As it will be apparent soon, these differences strongly affect the outcome of the dynamics.

Figure 1 compares the ADC(2) (red) and B3LYP (green) absorption spectra computed using the lowest 10 states listed in Table 1 with the experimental spectrum.[60] The spectra were obtained using the excitation energies and oscillator strengths calculated from the initial conditions obtained from Eq. (1). The lines were uniformly broadened by a Lorentzian function with a width of 0.1 eV.[59] To facilitate the comparison with the experiment, the intensities were scaled to one. Both computational methods give a similar absorption spectrum, with the band center at ≈ 6.2 eV. This is blueshifted by ≈ 0.2 eV with respect to the experimental spectrum, despite being $0.1-0.15$ eV lower than the vertical excitation energy of the bright state.

3.2 N-H bond dissociation on the $S_1(\pi\sigma^*)$ surface

The presence of a small exit barrier on the $A_2(\pi\sigma^*)$ state is well established, both experimentally and theoretically.[7,10] In agreement with a previous TD-PBE0 nonadiabatic dynamics study, we found that TDDFT underestimates the barrier height and in many cases even fails to locate a minimum on the $S_1(\pi\sigma^*)$ surface leading to internal conversion on a very short time scale.[14] Thus, we report only the ADC(2)/aug-cc-pVDZ results in this section. Figure 2 displays the ADC(2) potential energy profiles of the ground and the five lowest singlet excited electronic states along the N-H stretching coordinate. The potential energy cuts were obtained by a constrained relaxed scan along the N-H bond in the $S_1(\pi\sigma^*)$ state. The two states with $\pi\sigma^*$ character, $A_2(\pi\sigma^*)$ and $B_1(\pi\sigma^*)$ (S_5 at the $A_2(\pi\sigma^*)$ minimum energy geometry), are dissociative with respect to the N-H stretch coordinate, while the others are bound states strongly destabilized by the elongation of the N-H bond. Until reaching bond lengths close to the conical intersection,

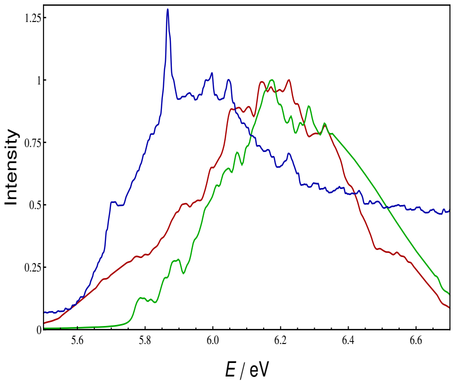

Fig. 1 Comparison of the simulated (scaled) and experimental (scaled, blue) spectra of pyrrole in the region between 5.5 and 6.7 eV corresponding to the first absorption band in the electronic spectrum.[60] Computations performed using the ADC(2)/aug-cc-pVDZ (red) and B3LYP/def2-TZVPD (green) methods. Transitions to the lowes t 10 electronic states listed in Table 1 are included.

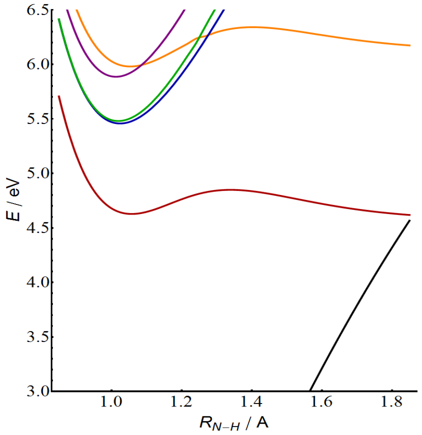

Fig. 2 Relaxed energy scan (in eV) along the N-H stretching coordinate optimized in the $A_2(\pi\sigma^*)$ state (red) using ADC(2)/aug-cc-pVDZ. Vertical excitation energies (ascending order) of the $A_2(\pi Ryd)$ (blue), $B_1(\pi Ryd)$ (green), $B_2(\pi\pi^*)$ (magenta) and $B_1(\pi\sigma^*)$ (orange) states and the energies of the ground state (black) are given.

these states have mostly ($> 90\%$) single excitation character and the ground state is not multireferent ($D1 < 0.04$). The scan reveals a barrier of $E_0 = 1780$ cm^{-1} in good agreement with previous CASSCF, MRCI and CASPT2/SA-CASSCF calculation yielding barriers of 2090, 1935 and 1615 cm^{-1}, respectively.[8,10,13]

The energy window centered at 250 nm addresses the minimum of the $A_2(\pi\sigma^*)$ surface and the energy imparted to the system is not enough to overcome the exit barrier shown in Figure 2. It goes without saying that in such conditions NA dynamics, in which the nuclei are treated classically, is inadequate for describing the dynamics. Indeed, in a test run, only a small fraction of trajectories ($< 10\%$) deactivated to the ground electronic state within the simulation time of 500 fs indicating a correct sampling of the initial conditions. Therefore, the standard WKB approach to tunnelling was used to estimate the KIE. In case of pyrrole, the generally multidimensional H-tunnelling dynamics can be approximated by 1D motion through the barrier.[62–64] Assuming the reduced masses of the N-H and N-D fragments as effective mass parameters,[65] the eigenstates of the relaxed 1D $A_2(\pi\sigma^*)$ potential were computed by diagonalizing the Hamiltonian with the Lanczos-Arnoldi integration scheme[66–68] implemented in the MCTDH program package.[69,70] Quasi-bound states were found at $E_0^H = 897.9$ and $E_0^D = 795.4$ cm^{-1} in case of pyrrole and pyrrole-d_1, respectively. The tunnelling probabilities were computed as $P = e^{2S}$ where S is the classical action integral through the barrier. The KIE was obtained as the ratio of hydrogen *vs* deuterium tunnelling probabilities. The semiclassical solution yields an isotope effect of $KIE = 9.9$, in very good agreement with the experimentally determined value of $KIE = 11$.[7]

Focusing on the experiments performed at 238 nm (5.21 eV), from Table 1 it is apparent that they interrogate the portion of the $S_1(\pi\sigma^*)$ surface to the blue from the vertical excitation. Most of the 100 trajectories started in the wavelength range $236 < \lambda < 240$ resulted in a fast and efficient relaxation to the ground state through N-H bond dissociation. The time dependent populations of the excited $S_1(\pi\sigma^*)$ state is shown in Figure 3. The calculated time constant for the depopulation of the S_1 state of 28 fs is in good agreement with the experimentally reported value of 46 ± 22, and the yield of 86% shows that the excitation energy in this window is enough to overcome the dissociation barrier.

To demonstrate the quality of the ADC(2) $A_2(\pi\sigma^*)$ surface a representative nonadiabatic trajectories is analyzed in Figure S1. For a set of geometries along the trajectory the D1 diagnostic for the reference MP2 ground state has been computed. D1 values greater that 0.04 indicate the break down of the single-reference approximation. As can be seen D1 values greater than 0.04 are found only in the close proximity of the $S_0/A_2(\pi\sigma^*)$ CI.

The common practice is to stop dynamics calculations when the energy gap between S_1 and S_0 drops below 0.1 eV.[46] In this way, errors of the method at distances beyond the CI do not impact the results of the dynamics. The high velocity of the hydrogen atom upon reaching the CI results in the formation of a ground state pyrrolyl radical and a hydrogen atom and no bifurcation takes place at the $S_0/A_2(\pi\sigma^*)$ CI. In this

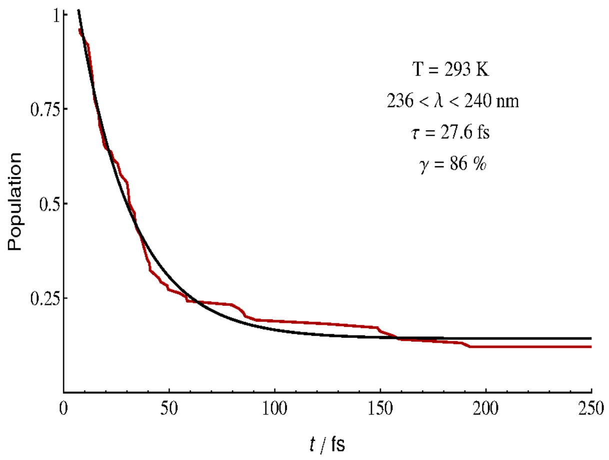

Fig. 3 Average population of the S_1 state of pyrrole obtained with NA dynamics simulations performed at $T = 293$ K in the wavelength range $236 < \lambda < 240$. The black line represents a mono-exponential fit for the decay of the S_1 state. The decay time constants (τ) and deactivation yield (γ) are given in the inset. Calculations were performed using the ADC(2)/aug-cc-pVDZ method.

wavelength range, this has been demonstrated through the total kinetic energy release spectra, which do not show a signal corresponding to the formation of an excited state radical, and time-resolved photoelectron spectra, both revealing only one time constant.[2,7,9] Taking this information into account, the time constant for reaching the $S_0/A_2(\pi\sigma^*)$ CI calculated by fitting the time-dependent population of the $A_2(\pi\sigma^*)$ state to a mono-exponential decay function is a good approximation of the time scale for the dissociation of the N-H bond, and thus can be directly compared to the experimental time constants from the measured H^+ signal as a function of increasing pump-probe delay.

Further, the CASPT2/aug-cc-pVDZ method has been used to check the accuracy of the ADC2(2)/aug-cc-pVDZ $A_2(\pi\sigma^*)$ surface. Figure S1 (lower panel) compares CASPT2 and ADC(2) excitation energies for a set of 11 geometries along a characteristic trajectory. It is evident that the two sets of calculations follow the same trend and with respect to exciation energies agree very well along the whole trajectory.

3.3 Dynamics initiated in the $B_2(\pi\pi^*)$ state

As pointed out, following excitation at 200 nm where the $B_2(\pi\pi^*)$ state is the dominant absorbing state, pyrrole undergoes a biexponential relaxation on the time scales of $\tau_1 = 52 \pm 12$ fs and $\tau_2 = 1.0 \pm 0.4$ ns.[7] The relaxation from the $B_2(\pi\pi^*)$ state was simulated in the wavelength range of $202 - 198$ nm mainly at the ADC(2)/aug-cc-pVDZ and B3LYP/def2-TZVPD levels.

NA dynamics simulations performed at the ADC(2)/aug-cc-pVDZ level found that 82% of the trajectories deactivated to the ground electronic state within the simulation time of 500 fs. Of these, 70% deactivated through N-H bond dissociation while the remaining trajectories deactivated *via* ring deformation. The calculated time constant for the dominant N-H bond dissociation pathway (also for the non-reactive pathway) is greater than 150 fs which is about three times longer than the experimental value of 52 ± 12 fs. Increasing the size of the basis set (cc-pVTZ+) or considering higher energies ($198 - 196$) had very little influence on the results. Our ADC(2) results find agreement with previous MR-CISD+Q and TDDFT(PBE0)-based NA dynamics simulations reporting time constants of ≈ 140 and ≈ 180 fs,[13,14] indicating that a systematic problem affects the simulation of the dynamics from the $B_2(\pi\pi^*)$ state.

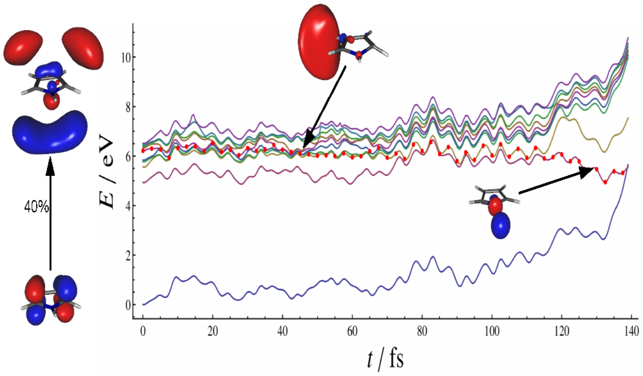

Fig. 4 Time dependence of the potential energy of the electronic ground state and 9 excited states (for initial states, see Table 1.) for a selected non-adiabatic trajectory as computed using ADC(2)/aug-cc-pVDZ. Red circles indicate the populated state at a given time. The trajectory is initiated in the state with the largest oscillator strength. Inset (left) HF occupied and virtual MO corresponding to the dominant orbital transition (40%) at the initial geometry. Insets (middle, right) HF virtual MO corresponding to dominant orbital transition for electronic states encountered in the dynamics.

The origin of the problem can be inferred from Figure 4 where the time evolution of a characteristic NA trajectory initiated in the S_5 state is shown. The variation of the potential energy of the ground and 9 excited electronic states is shown with the electronic state in which the trajectory resides marked with red circles. As mentioned, the dominant (40%) single-orbital transition of the bright B_2 state is of π-Rydberg character as shown in the inset of Figure 4. Due to strong Rydberg-valence interaction, frequent hops between this state and other mixed Rydberg states occur during the dynamics. As a result, the system evolves on what is basically an averaged potential energy surface.

At the B3LYP/def2-TZVPD level N-H bond dissociation was found again to be the dominant deactivation mechanism, while ring puckering occurred only in 6% of the cases. In sharp contrast to ADC(2)/aug-cc-pVDZ results, the B3LYP/def2-TZVPD dynamics leads to fast excited state deactivation. The timescale of N-H bond dissociation has been computed as a monoexponential fit of the total depopulation of the excited states for trajectories ending in dissociation. The computed time constant of $\tau = 48$ fs, which accounts only for the trajectories leading to N-H bond fission, is in excellent agreement with the measurement of Roberts *et. al.*[7] Note also that within the 250 fs long simulation time a complete (98%) deactivation to the ground state has occurred.

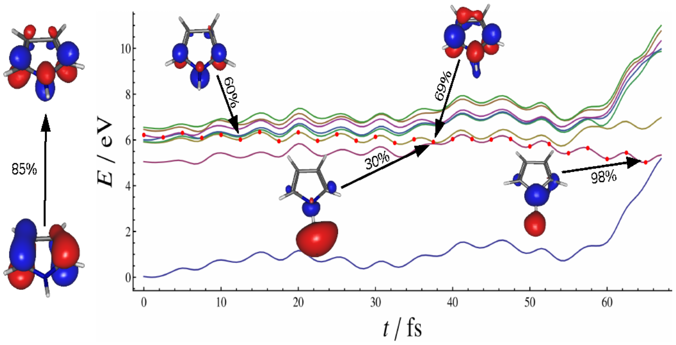

Fig. 5 Time dependence of the potential energy of the electronic ground state and 7 excited states (for initial states, see Table 1.) for the selected non-adiabatic trajectory as computed using B3LYP/def2-TZVPD. Red circles indicate the populated state at a given time. The trajectory is initiated in the $B_2(\pi\pi^*)$ state. Inset (left) KS occupied and virtual MO corresponding to the dominant orbital transition (89%) at the initial geometry. Insets (middle, right) KS virtual MO corresponding to dominant orbital transitions for electronic states encountered in the dynamics.

A typical B3LYP/def2-TZVPD trajectory deactivating through N-H bond dissociation is shown in Figure 5. The simulation started from the $B_2(\pi\pi^*)$ state which is the adiabatic S_5 state. As in the ADC(2) case, the $B_2(\pi\pi^*)$ state is intercalated in a dense manifold of excited states and two Rydberg states are found lower in energy. However, the valence and Rydberg states are separated and the initial excitation is of clear $\pi\pi^*$ character as shown in the insets (left) of Figure 5. During the dynamics, the system evolves through out-of-plane motions towards the minimum of the state. At the geometry of the minimum, the $B_2(\pi\pi^*)$ state is the second adiabatic state. Since there is very little mixing between the $B_2(\pi\pi^*)$ state and the Rydberg states, no hops occur to those states as the system evolves past them. The change of character of the excitation occurs in the vicinity of the $B_2(\pi\pi^*)/A_2(\pi\sigma^*)$ CI which is reached at $\tau_1 \approx 28$ fs. The subsequent dynamics on the $A_2(\pi\sigma^*)$ surface is driven by N-H bond elongation as described in Sec. 3.2.

Note that a similar deactivation dynamics is not possible at the ADC(2)/aug-cc-pVDZ level because in this case the minimum of the B_2 state is planar and higher in energy than some of the Rydberg states. Thus the shorter relaxation time computed with B3LYP/def2-TZVPD directly reflects the topography of the $B_2(\pi\pi^*)$ state.

To check that the slow and fast relaxation dynamics obtained with ADC(2)/aug-cc-pVDZ and B3LYP/def2-TZVPD methods, respectively, are not consequences of dynamics simulations being run in regions of configurational space where the two methods are not applicable, the D1 and λ parameters have been monitored along the respective trajectories. From Figs. S2 and S3 it can be seen that both parameters are in the aceptable range. Further, the excitation energies of the adiabatic electronic state in which the molecule resides during the dynamics have been compared with respective CASPT2 values. For the ADC(2) and TD-B3LYP trajectories shown in Figures 4 and 5, the comparison with CASPT2/aug-cc-pVDZ excitation energies are displayed in the lower panels of Figures S2 and S3, respectively. It is evident that a very good agreement with the referent CASPT2 values is obtained for both sets of geometries. Apart from the ADC(2) geometry at $t = 13$ fs, the two sets of energy data are close and parallel to each other. This is particularly true for the B3LYP/def2-TZVPD values. Therefore the computed difference in relaxation dynamics is not due to erroneous energetics of the states, but stems from different Rydberg-valence interactions that shape the potential energy surfaces. Because of strong Rydberg-valence mixing the deplanarization of the pyrrole ring along the ADC(2)/aug-cc-pVDZ trajectory destabilizes the system and takes place only after internal conversion to the dissociative $\pi\sigma^*$ states. In other words the system explores only a limited portion of the potential energy surface and in this region the agreement with CASPT2 values is very good. On the other hand, deplanarization of the ring is favored on the B3LYP/def2-TZVPD surface and the trajectory encounters the conical intersection with the lowest $\pi\sigma^*$ state at earlier times.

To further test this claim, NA dynamics simulations were performed using two additional basis sets at the TDDFT level. The def2-QZVP(-f,-g) basis set provides a similar description of valence states to def2-TZVPD, but due to the lack of diffuse functions, Rydberg states are destabilized with this basis set and located above the $B_2(\pi\pi^*)$ state. The dynamics with these two basis sets are similar ($\tau = 44$ fs *vs* 48 fs), showing that the Rydberg states have relatively little influence on the dynamics. On the other hand, mixing between valence and Rydberg states is present at the B3LYP/aug-cc-pVTZ level and the NA dynamics results are similar to those obtained with the ADC(2) method ($\tau > 200$ fs).

Altogether, our NA dynamics calculations indicate that the observed ultrafast relaxation from the $B_2(\pi\pi^*)$ state is compatible with only a low degree of mixing between the $B_2(\pi\pi^*)$ and Rydberg states which results in the stabilization of the $B_2(\pi\pi^*)$ minimum below the Rydberg manifold.

4 Conclusion

Nonadiabatic dynamics simulations were performed for pyrrole at the ADC(2) and TDDFT (B3LYP) level. The salient points of our study on the dynamics of H-elimination from pyrrole are the following.

(i) At the ADC(2)/aug-cc-pVDZ level, a barrier of 1780 cm^{-1} has been computed in the $A_2(\pi\sigma^*)$ state along the N-H stretching coordinate resulting in the formation of a quasi-bound state. Accordingly, the dynamics of H-elimination after excitation to the origin of S_1 is driven by tunnelling. A semiclassical kinetic isotope effect of $KIE = 9.9$ was computed, in very good agreement with the experimentally determined value.

(ii) After excitation to the $A_2(\pi\sigma^*)$ state in the wavelength range of $236-240$ nm, i.e., on the blue side from the vertical excitation, the dissociation of the N-H bond can be described by trajectory-based dynamics. At $T = 293$ K we computed a time constant of 28 fs, in good agreement with the recently determined experimental value.

(iii) A complex dynamical behavior is encountered upon excitation to the $B_2(\pi\pi^*)$ state. In the $198-202$ nm range the computed time constant for H-elimination of 48 fs obtained using the B3LYP/def2-TZVPD method finds very good agreement with the experiment, a significant improvement over previous dynamics simulations performed from the $B_2(\pi\pi^*)$ state. This is attributed to the correct topography of the state and lack of mixing between the $\pi\pi^*$ state and the $3p_x$ Rydberg state which occurs in a number of other methods (including ADC(2)/aug-cc-pVDZ used in this work).

The presented results on the photorelaxation dynamics of pyrrole succeeded in reproducing and explaining recent experimental results. It was shown that vertical excitation energies by themselves are not a sufficient criterium for successful nonadiabatic dynamics calculations in pyrrole. Instead, the main requirements are a correct barrier on the $A_2(\pi\sigma^*)$ and the character of the $B_2(\pi\pi^*)$ state. In our work these requirements could only be met by using different methods for the different wavelength ranges. For pyrrole, similar problems were encountered by other researchers,[39] indicating that advances in electronic structure methods are needed in order to achieve an accurate description of pyrrole excited states. From the experimental side, time resolved photoelectron imaging experiments may be able to provide an additional level of information on the effect of Rydberg-valence mixing on the $B_2(\pi\pi^*)$ equilibrium structure and dynamics of H-elimination.

5 Acknowledgment

The authors thank Milena Petković and Ivan Ljubić for helpful discussion. The research was supported by the Unity through Knowledge Fund (UKF B1). The authors acknowledge generous computer time provided by the Croatian National Grid Infrastructure (CRONGI).

References

1 A. R. Battersby, *Nat. Prod. Rep.*, 2000, **17**, 507–526.

2 B. Cronin, M. G. D. Nix, R. H. Qadiri and M. N. R. Ashfold, *Phys. Chem. Chem. Phys.*, 2004, **6**, 5031–5041.

3 J. Wei, J. Riedel, A. Kuczmann, F. Renth and F. Temps, *Faraday Discuss.*, 2004, **127**, 267–282.

4 H. Lippert, H. H. Ritze, I. V. Hertel and W. Radloff, *ChemPhysChem*, 2004, **5**, 1423–14277.

5 B. Cronin, A. L. Devine, M. G. D. Nix and M. N. R. Ashfold, *Phys. Chem. Chem. Phys.*, 2006, **8**, 3440–3445.

6 R. Montero, A. P. Conde, V. Ovejas, M. Fernández-Fernández, F. Castano, J. R. V. de Aldana and A. Longarte, *J. Chem. Phys.*, 2012, **137**, 064317/1–8.

7 G. M. Roberts, C. A. Williams, H. Yu, A. S. Chatterley, J. D. Young, S. Ullrich and V. G. Stavros, *Faraday Discuss.*, 2013, **163**, 95–116.

8 T. N. V. Karsili, B. Marchetti, R. Moca and M. N. R. Ashfold, *J. Phys. Chem. A*, 2013, **117**, 12067–12074.

9 G. Wu, S. P. Neville, O. Schalk, T. Sekikawa, M. N. R. Ashfold, G. A. Worth and A. Stolow, *J. Chem. Phys.*, 2015, **142**, 074302/1–12.

10 V. Vallet, Z. Lan, S. Mahapatra, A. L. Sobolewski and W. Domcke, *Faraday Discuss*, 2004, **127**, 283–293.

11 V. Vallet, Z. Lan, S. Mahapatra, A. L. Sobolewski and W. Domcke, *J. Chem. Phys*, 2005, **123**, 144307/1–15.

12 I. Frank and K. Damianos, *J. Chem. Phys.*, 2007, **126**, 125105/1–5.

13 M. Vazdar, M. Eckert-Maksić, M. Barbatti and H. Lischka, *Mol. Phys.*, 2009, **107**, 845–854.

14 M. Barbatti, J. Pittner, M. Pederzoli, U. Werner, R. Mitrić, V. Bonačić-Koutecký and H. Lischka, *Chem. Phys.*, 2010, **375**, 26–34.

15 S. Faraji, M. Vazdar, V. S. Reddy, M. Eckert-Maksić, H. Lischka and H. Köppel, *J. Chem. Phys.*, 2011, **135**, 154310/1–13.

16 K. Saita, M. G. D. Nix and D. V. Shalashilin, *Phys. Chem. Chem. Phys.*, 2013, **15**, 16227–16235.

17 A. L. Sobolewski and W. Domcke, *Chem. Phys.*, 2000, **259**, 181–191.

18 A. L. Sobolewski, W. Domcke, C. Dedonder-Lardeux and C. Jouvet, *Phys. Chem. Chem. Phys.*, 2002, **4**, 1093–1100.

19 M. Ashfold, B. Cronin, A. L. Devine, R. Dixon and M. G. D. Nix, *Science*, 2006, **312**, 1637–1640.

20 G. M. Roberts and V. G. Stavros, *Chem. Sci.*, 2014, **5**, 1698.

21 O. Christiansen, J. Gauss, J. F. Stanton and P. Jørgensen, *J. Chem. Phys*, 1999, **111**, 525–537.

22 B. O. Roos, P.-A. Malmqvist, V. Molina, L. Serrano-Andrés and M. Merchán, *J. Chem. Phys.*, 2002, **116**, 7526–7536.

23 X. Li and J. Paldus, *J. Phys. Chem. A*, 2010, **114**, 8591–8600.

24 P. Celani and H.-J. Werner, *J. Chem. Phys*, 2003, **119**, 5044–5057.

25 D. J. Tozer, R. D. Amos, N. C. Handy, B. . Roos and L. Serrano-Andrés, *Mol. Phys.*, 1999, **97**, 859–868.

26 J. Schirmer, *Phys. Rev. A*, 1982, **26**, 2395–2416.

27 A. B. Trofimov and J. Schirmer, *J. Phys. B*, 1995, **28**, 2299–2324.

28 TURBOMOLE V6.4 2012, a development of University of Karlsruhe and Forschungszentrum Karlsruhe GmbH, 1989-2007, TURBOMOLE GmbH, since 2007, available from http://www.turbomole.com.
29 C. Hättig and F. J. Weigend, *J. Chem. Phys.*, 2000, **113**, 5154–5161.
30 F. Weigend, A. Köhn and C. Hättig, *J. Chem. Phys.*, 2002, **116**, 3175.
31 C. Hättig, A. Hellweg and A. Köhn, *Phys. Chem. Chem. Phys.*, 2006, **8**, 1159–1169.
32 A. D. Becke, *J. Chem. Phys.*, 1993, **98**, 5648–5652.
33 C. Hättig, *Advances in Quantum Chemistry*, 2005, **50**, 37–60.
34 M. Barbatti and R. Crespo-Otero, *Top. Curr. Chem.*, 2015.
35 C. L. Janssen and I. M. Nielsen, *Chem. Phys. Lett.*, 1998, **290**, 423–430.
36 M. J. G. Peach, P. Benfield, T. Helgaker and D. J. Tozer, *J. Chem. Phys.*, 2008, **128**, 044118/1–8.
37 K. Aidas et al., *WIREs Comput. Mol. Sci.*, 2014, **4**, 269–284.
38 Dalton, a molecular electronic structure program, Release Dalton2015.X (2015), see http://daltonprogram.org.
39 S. P. Neville and G. A. Worth, *J. Chem. Phys.*, 2014, **140**, 034317/1–13.
40 K. Kaufmann, W. Baumeister and M. Jungen, *J. Phys. B: At. Mol. Opt. Phys.*, 1989, **22**, 2223–2240.
41 I. Ljubić and A. Sabljić, *J. Phys. Chem. A*, 2011, **115**, 4840–4850.
42 D. Rappoport and F. Furche, *J. Chem. Phys.*, 2010, **133**, 134105/1–11.
43 T. H. Dunning, *J. Chem. Phys.*, 1989, **90**, 1007–1023.
44 H. Werner, P. J. Knowles, G. Knizia, F. R. Manby and M. Schütz, *Wiley Interdisciplinary Reviews: Computational Molecular Science*, 2012, **2**, 242–253.
45 J. C. Tully, *J. Chem. Phys.*, 1990, **93**, 1061–1071.
46 F. Plasser, R. Crespo-Otero, M. Pederzoli, J. P. H. Lischka and M. Barbatti, *J. Chem. Theory Compt.*, 2014, **10**, 1395–1405.
47 E. Tapavicza, I. Tavernelli and U. Rothlisberger, *Phys. Rev. Lett.*, 2007, **98**, 023001/1–4.
48 I. Tavernelli, E. Tapavicza and U. Rothlisberger, *J. Chem. Phys.*, 2009, **130**, 124107/1–10.
49 I. Tavernelli, B. F. E. Curchod and U. Rothlisberger, *J. Chem. Phys.*, 2009, **131**, 196101/1–2.
50 S. Hammes-Schiffer and J.C.Tully, *J. Chem. Phys.*, 1994, **101**, 4657–4667.
51 U. Werner, R. Mitrić, T. Suzuki and V. Bonačić-Koutecký, *Chem. Phys.*, 2008, **349**, 319–324.
52 J. Novak, M. Mališ, A. Prlj, I. Ljubić, O. Kühn and N. Došlić, *J. Phys. Chem. A*, 2012, **116**, 11467–11475.
53 M. Mališ, Y. Loquais, E. Gloaguen, C. Jouvet, V. Brenner, M. Mons, I. Ljubić and N. Došlić, *Phys. Chem. Chem. Phys.*, 2014, **16**, 2285–2288.
54 L. Shampine and M. Gordon, *Computer Solution of Ordinary Differential Equations: The Initial Value Problem*, Freeman, 1975.
55 R. Mitrić, U. Werner and V. Bonačić-Koutecký, *J. Chem. Phys.*, 2008, **129**, 164118/1–9.
56 J. Tannor, David, *Introduction to quantum mechanics: a time-dependent perspective*, University Science Books, Sausalito, CA, 2007.
57 N. Došlić and S. Bosanac, *Mol. Phys.*, 1997, **90**, 599–609.
58 L. Sun and W. L. Hase, *J. Chem. Phys.*, 2010, **133**, 044313/1–9.
59 M. Barbatti, A. J. A. Aquino and H. Lischka, *Phys. Chem. Chem. Phys.*, 2010, **12**, 4959–4967.
60 M. H. Palmer, I. C. Walker and M. F. Guest, *Chem. Phys.*, 1998, **238**, 179–199.
61 M. H. Palmer and J. P. Wilson, *Mol. Phys.*, 2003, **101**, 2391–2408.
62 K. Giese, M. Petković, H. Naundorf and O. Kühn., *Phys. Rep.*, 2006, **430**, 211–276.
63 I. Matanović, N. Došlić and O. Kühn., *J. Chem. Phys.*, 2007, **127**, 014309–7.
64 M. Mališ, Y. Loquais, E. Gloaguen, H. Biswal, F. Piuzzi, B. Tardivel, V. Brenner, M. Broquier, C. Jouvet, M. Mons, N. Došlić and I. Ljubić, *J. Am. Chem. Soc.*, 2012, **134**, 20340–20351.
65 M. Petković, J. Novak and N. Došlić, *Chem. Phys. Lett.*, 2009, **474**, 248–252.
66 W. E. Arnoldi, *Quart. Appl. Math.*, 1951, **9**, 17–29.
67 Y. Saad, *Linear Algebra Appl.*, 1980, **34**, 269–295.
68 R. A. Friesner, L. S. Tuckerman, B. C. Dornblaser and T. V. Russo, *J. Sci. Comput.*, 1989, **4**, 327–354.
69 G. A. Worth, M. H. Beck, A. Jäckle and H.-D. Meyer, The MCTDH Package, Version 8.2, (2000). H.-D. Meyer, Version 8.3 (2002), Version 8.4 (2007). See http://mctdh.uni-hd.de.
70 M. H. Beck, A. Jäckle, G. Worth and H.-D. Meyer, *Phys. Rep.*, 2000, **324**, 1–105.

6 Graphics and tables

6.1 Tables

Table 1 Comparison between the B3LYP/def2-TZVPD and ADC(2)/aug-cc-pVDZ vertical and (adiabatic) excitations for pyrrole with previously reported values. Computed oscillator strengths are given in square brackets where available.

State	B3LYP[a]	ADC(2)[a]	GMS CC SD[b]	MS-CASPT2[c]	CASPT2 / MCTDH[d]	Experimental[e,f]
$A_2(\pi\sigma^*)$	4.99	5.13 (4.82)	5.10	5.22	5.06	5.22
	[0.000]	[0.000]		[0.000]		
$B_1(\pi\sigma^*)$	5.87	5.75 (5.57)	5.79		5.86	
	[0.013]	[0.013]				
$A_2(3p_z)$	5.89	5.86	5.81	5.97	5.87	
	[0.000]	[0.000]		[0.000]		
$B_1(3p_y)$	5.95	5.89	5.96	5.87	6.00	5.85
	[0.026]	[0.031]		[0.026]		
$B_2(\pi\pi^*)$	6.32 (5.62)	6.35 (6.01)	5.96	5.87	6.24	5.90
	[0.174]	[0.214]		[0.209]		
$A_1(\pi\pi^*)$	6.47	6.49	6.53	5.82	6.01	
	[0.001]	[0.000]		[0.036]		
$A_2(\pi Ryd)$	6.54	6.44	6.38			
	[0.001]	[0.000]				
$B_1(\pi Ryd)$	6.57	6.44	6.40			
	[0.001]	[0.000]				
$B_1(3p_z)$	6.77	6.59	6.65			
	[0.001]	[0.000]				
$A_2(3p_y)$	6.89	6.65	6.45			
	[0.001]	[0.000]				

[a]Present work, [b]Reference[23], [c]Reference[22], [d]Reference[39], [e]Reference[60], [f]Reference[61]